High-speed solar wind streams in 2007-2008: Turning on the Russell-McPherron effect

C. Munteanu[1], A. Hamada[2], and K. Mursula[2]

[1]Institute of Space Science, Măgurele, Romania

[2]ReSoLVE Centre of Excellence, Space Climate Research Unit, University of Oulu, Oulu, Finland

Key Points:

- We study two sequences of stable high-speed streams with opposite polarities in 2007-2008, locate their sources and follow their effects.
- IMF Bz(GSM)-Bz(GSE) difference decreases (increases) systematically in the negative (positive) polarity sequence from solstice to equinox.
- We quantify the effect of this turning on of the Russell-McPherron mechanism to high-latitude geomagnetic activity and geomagnetic storms.

Corresponding author: Costel Munteanu, `costelm@spacescience.ro`

This article has been accepted for publication and undergone full peer review but has not been through the copyediting, typesetting, pagination and proofreading process which may lead to differences between this version and the Version of Record. Please cite this article as doi: 10.1029/2019JA026846

Abstract

Two sequences of five high-speed solar wind stream/corotating interaction region (HSS/CIR) events were observed at 1 AU in December 2007 - April 2008. These two HSS/CIR sequences had opposite magnetic polarities and they originated from two persistent low-latitude coronal holes with corresponding polarities. Each HSS/CIR event triggered a geomagnetic storm and strong high-latitude activity. We follow the evolution of the properties and geomagnetic effects of the two sequences, and find that the sequence with negative IMF polarity (toward sector) develops systematically a more negative Bz(GSM) component and becomes relatively more geoeffective when moving from winter solstice in 2007 to spring equinox in 2008. On the other hand, the sequence with positive polarity (away sector) develops systematically a less negative Bz(GSM) component and becomes relatively less geoeffective. These changes allow the first detailed monitoring of the turning on of the Russell-McPherron effect when moving from solstice to equinox, and the development of the related changes in high-latitude geomagnetic activity and geomagnetic storms.

1 Introduction

During the late declining phase of solar cycle 23, the near-Earth solar wind was dominated by high-speed streams (HSSs) and their associated stream interaction regions (SIRs), intervals of increased plasma density and magnetic field magnitude (see, e.g., Mason et al., 2009; Gibson et al., 2011). An SIR is formed when a fast solar wind emanating from a coronal hole (CH) runs into the slower solar wind ahead of it. SIRs which repeat in several solar rotations, are called corotating interaction regions (CIRs) (see, e.g., Gosling & Pizzo, 1999; Richardson, 2018).

Abramenko et al. (2010) studied the low- and mid-latitude CHs observed on the Sun around the 2008 solar minimum, and found a recurrent appearance of two persistent CHs with opposite magnetic polarities, with the most long-lived CH lasting for 27 rotations. de Toma (2011) also studied the CHs observed during this period, and showed that large and long-lived low- and mid-latitude CHs were present on the Sun until the end of 2008, and remained important sources of recurrent high-speed solar wind streams.

HSSs/SIRs are the dominant source of geomagnetic disturbances during several years around solar minima (Alves et al., 2006; Tsurutani et al., 2006; Holappa et al., 2014).

HSSs/SIRs often produce minor geomagnetic storms and high-intensity, long-duration, continuous AE activity (HILDCAA) events (Tsurutani & Gonzalez, 1987; Hajra et al., 2013). HILDCAAs mainly occur in the recovery phase of the magnetic storm, have a peak AE index value greater than 1000 nT and a duration of at least 2 days long. There are also numerous thermospheric and ionospheric effects related to HSSs/SIRs (Tulasi Ram et al., 2010a, 2010b; Lei et al., 2011; Wang et al., 2011; Verkhoglyadova et al., 2011, 2013; McGranaghan et al., 2014).

The time period of March 20 - April 16, 2008 (Carrington rotation 2068), known as the whole heliosphere interval (WHI), was an interval of an international campaign to study the three-dimensional solar-heliospheric-planetary system near the solar minimum (Gibson et al., 2009; Maris & Maris, 2009; Gibson et al., 2011; Thompson et al., 2011; Webb et al., 2011; Echer et al., 2011). Gibson et al. (2011) presented an overview of observations from the Sun's interior to the near-Earth space in 2008-2009. They showed that two long-lived, low-latitude CHs were observed on the Sun during the WHI interval, one having a positive polarity, the other a negative-polarity. (The magnetic field has a positive polarity, an away sector, when the magnetic field lines are directed away from the Sun, and a negative polarity, a toward sector otherwise). They also showed that, from mid-2008 onwards, these two CHs started fragmenting to a number of smaller CHs.

The geoeffectiveness of the solar wind is mainly controlled by the Bz(GSM) component of the IMF. The southward oriented (negative) IMF Bz(GSM) component causes large-scale reconnection of magnetic field lines at the dayside magnetosphere (Dungey, 1961), thus enhancing magnetospheric convection and energy transfer. Large values of negative Bz can occur, e.g., during magnetic clouds, in SIRs or other shocks (Lockwood et al., 2016; Kilpua et al., 2017). Moreover, a negative Bz(GSM) can be produced from the horizontal IMF component by the Russell-McPherron (R-M) mechanism (Russell & McPherron, 1973). According to the R-M effect, an away directed (positive polarity) IMF increases the geoeffectiveness of solar wind in the fall and reduces it in the spring, and vice versa for a toward directed (negative polarity) IMF. This connection between IMF polarity and geoeffectiveness was used by Russell and McPherron (1973) to give a new explanation for the observed semiannual variation of geomagnetic activity. The two earlier proposed mechanisms are the axial mechanism (Cortie, 1912; Bohlin, 1977), and the equinoctial mechanism (Bartels, 1932; McIntosh, 1959; Boller & Stolov, 1970; Lyatsky et al., 2001; Newell et al., 2002). Although some studies (Cliver et al., 2000) suggest that the equinoctial mechanism is the dominant mechanism, other studies (Mursula et al., 2011; Tanskanen et al., 2017) denounce most of the earlier studies and argue that the final conclusion on the semiannual variation in geomagnetic activity must still be awaited.

Crooker and Cliver (1994) were among the first to demonstrate that the level of recurrent and sustained activity associated with HSSs/CIRs is controlled by the R-M effect. Crooker (2000) studied the R-M effect in two geomagnetic storms observed during spring 1997, showing that the storm generated by a negative-polarity high-speed stream was stronger than the one generated by a positive-polarity stream. McPherron et al. (2009) showed that, around equinoxes, the R-M effect strongly controls whether or not a given high-speed stream is geoeffective, especially in terms of relativistic electrons. They showed that the more geoeffective high-speed streams have twice as strong geomagnetic activity and an order of magnitude higher electron fluxes than the less geoeffective streams.

Maris and Maris (2009) studied the HSSs during three Carrington rotations around the WHI interval. They showed that a two-stream structure with opposite polarities is dominant during this period. They detected two minor storms during this period, both of them associated with negative polarity streams. However, they did not associate this increased geoeffectiveness of the negative polarity streams with the R-M effect. Lei et al. (2011) also showed that the high-speed stream of the WHI interval from the CH with negative polarity was more geoeffective than the stream with positive polarity, both in terms of geomagnetic activity as well as of the thermospheric density response. Echer et al. (2011) showed that the AE and Dst indices were larger for the first HSS, and noted that this difference is as expected from the R-M mechanism. They also noted that the two streams of the WHI interval recur during several rotations, but did not study their properties or geoeffectiveness beyond the one rotation of the WHI interval.

In this study we will analyse the geoeffectiveness of the two sequences of HSS/CIR events with opposite magnetic polarities, observed during the late 2007 and early 2008. We identify their coronal hole sources and study their temporal evolution. We calculate the distribution of several solar wind/IMF parameters and geomagnetic indices in order to quantitatively estimate the geoeffectiveness of each HSS/CIR event and to evaluate the temporally changing effect of the R-M mechanism. Many papers have discussed the R-M mechanism statistically (McPherron et al., 2009; Zhao & Zong, 2012; Miyoshi et al., 2013; McGranaghan et al., 2014) and some papers have even discussed the effect of the R-M mechanism to individual events (Crooker, 2000; Echer et al., 2011). However, there are no studies showing a systematic, opposite development of the IMF Bz-component in two HSS streams of opposite polarity and the related oppositely developing changes in geomagnetic activity over multiple solar rotations. In this paper, by following the repetition of two HSSs during five successive rotations, we are able to, first of all, follow the onset ("turning on") of the R-M effect leading to more negative Bz(GSM) in one stream and to less negative Bz(GSM) in the other stream, and secondly, to demonstrate systematic changes in geomagnetic activity that are convincingly proven to be only due to the changing Bz-component, and not due to the other geoeffective factors in the solar wind.

The paper is organised as follows. In Section 2 we present the datasets used in this study. In Section 3 we describe the large-scale solar wind conditions in late 2007 to early 2008 and identify the two HSS/CIR sequences and their individual HSS/CIR events. In Section 4 we discuss the solar sources of these solar wind streams. In Section 5 we compare the average properties of the two sequences using the superposed epoch method. Section 6 presents the geomagnetic activity associated with the observed HSS/CIR events. In Section 7 we follow the temporal evolution of the IMF Bz(GSM) component within the two sequences and quantify the Russell-McPherron effect to Bz(GSM) and the geomagnetic activity indices AE and SYM-H. We give our conclusions in Section 8.

2 Data sets used in this study

We use Carrington maps of the McIntosh Archive to study the evolution of coronal holes during December 2007 - April 2008. Each map depicts the coronal holes during one Carrington rotation, with negative polarity holes depicted in red, and the positive polarity holes in blue (Webb et al., 2017, 2018).

The solar wind parameters and geomagnetic indices used in this study were obtained from the NASA/NSSDC OMNI dataset at 1-minute time resolution. The OMNI dataset includes the geomagnetic SYM-H (symmetric disturbance) index, which measures the mean horizontal magnetic field deflection at low latitudes and, similarly to the Dst index, reflects the intensity of the symmetric part of the magnetospheric ring current (Iyemori et al., 2010). We also use the auroral electrojet (AE) index which reflects the ionospheric current intensity in the auroral zone (Davis & Sugiura, 1966).

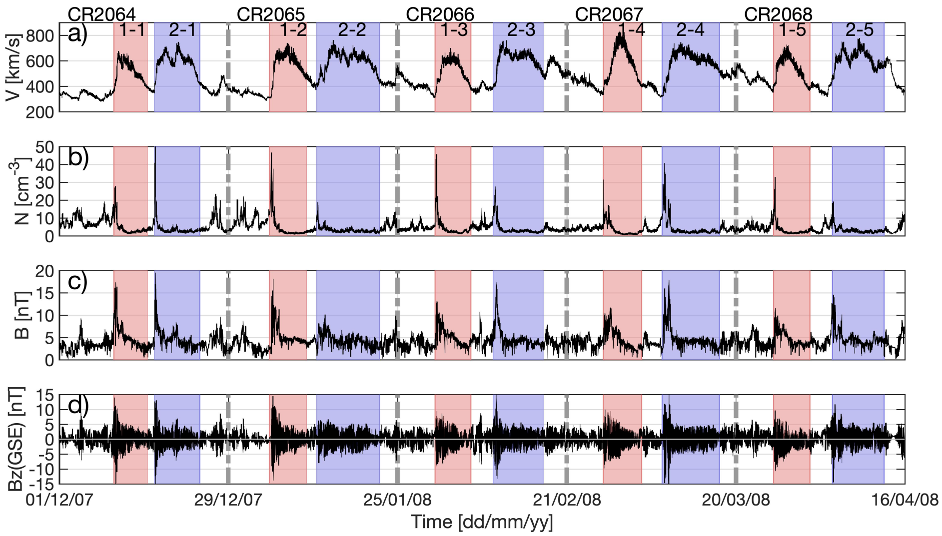

Figure 1. Solar wind parameters (1-min resolution) during December 2007 - April 2008. From top to bottom: solar wind speed, solar wind density, IMF magnitude and IMF Bz(GSE) component. HSS/CIR sequence 1 (2) is marked with red (blue) colour. Carrington rotations are marked with vertical dash-dotted bars.

3 HSS/CIR sequences

Figure 1 presents the solar wind speed and density, and the magnitude and z-component of the IMF during December 2007 - April 2008. One can clearly see the occurrence of several HSS/CIR events with their characteristic signatures: periods of fast solar wind, and peaks of large solar wind density and IMF magnitude associated with the increasing solar wind speed. A typical CIR at 1 AU has a leading edge of increased plasma density and compressed magnetic field, which passes the Earth in about one day. A high-speed stream follows thereafter and lasts for several days, during which the plasma density and the IMF magnitude drop to relatively low values. Each HSS/CIR event ends with a trailing edge, where the speed decreases to lower values.

The starting time of each HSS/CIR event was chosen to correspond to the abrupt increase in solar wind density (see, e.g., Vršnak et al., 2017). The end time of each event corresponds to the end of the period of high solar wind velocity and low solar wind density. Table 1 gives the start and end times of the ten HSS/CIR events. The time segment corresponding to each event is marked in Fig. 1 with colour. We have divided the ten HSS/CIR events into two sequences: sequence 1 marked in Fig. 1 with red colour,

Table 1. Times of the start of the leading edge, end of the trailing edge and the durations for the ten HSS/CIR events observed at 1AU in December 2007 - April 2008. Each HSS/CIR event is denoted with a two-digit label, where the first number (1 or 2) presents the HSS/CIR sequence and the second number (1-5) the order of the event within the sequence.

HSS/CIR	Start	End	Duration	Average duration
Event 1-1	2007-12-10 at 02pm	2007-12-16 at 12pm	05.42 days	
Event 1-2	2008-01-04 at 04pm	2008-01-10 at 04pm	06.00 days	(Sequence 1)
Event 1-3	2008-01-31 at 11am	2008-02-06 at 06am	05.79 days	05.86 $\pm$ 0.29 days
Event 1-4	2008-02-27 at 03pm	2008-03-04 at 08pm	06.21 days	
Event 1-5	2008-03-26 at 03am	2008-04-01 at 12pm	05.88 days	
Event 2-1	2007-12-17 at 03am	2007-12-24 at 10am	07.29 days	
Event 2-2	2008-01-12 at 07am	2008-01-22 at 12am	10.21 days	(Sequence 2)
Event 2-3	2008-02-09 at 07pm	2008-02-17 at 11pm	08.17 days	08.66 $\pm$ 1.11 days
Event 2-4	2008-03-08 at 03am	2008-03-17 at 09am	09.25 days	
Event 2-5	2008-04-04 at 03pm	2008-04-13 at 12pm	08.38 days	

and sequence 2 marked with blue. Figure 1 denotes each HSS/CIR event with a two-digit label, where the first number (1 or 2) presents the HSS/CIR sequence and the second number (1-5) the order of the event within the sequence. For example, the HSS/CIR events of the first rotation CR2064 are denoted by HSS/CIR1-1 and HSS/CIR2-1. The mean durations of the two HSS/CIR sequences are: 5.86 ± 0.29 days for sequence 1, and 8.66 ± 1.11 days for sequence 2. The shortest HSS/CIR event of sequence 1 is 5.42 days, and the longest event is 6.21 days. For sequence 2, the shortest HSS/CIR event is 7.29 days, and the longest event is 10.21 days.

Average time delays were calculated between the ten HSS/CIR events given in Table 1. The mean time delays are: 26.98 ± 1.07 days between the events of sequence 1, 9.33 ± 1.35 days between successive events of sequences 1 and 2, and 27.42 ± 0.96 days between the events of sequence 2. The time delay between the events of the same sequence is naturally associated with the solar rotation period. The time delays between successive events of sequences 1 and 2 were used in the identification of the corresponding CH sources.

Solar wind density (Fig. 1b) shows, in addition to the dominant peaks associated with the leading edges of sequences 1 and 2, also other (similarly repeating) minor peaks. These are located at about half-way between the dominant peaks, close to the CR change time (denoted by vertical bars in Fig. 1). There are also solar wind velocity enhancements and IMF peaks associated with these minor density peaks. These obviously form a sequence of weaker HSS/CIR events. We will discuss their source later, but we will not include them in our statistical analysis.

4 HSS sources

Figure 2 shows five synoptic (Carrington) maps of coronal holes from the McIntosh archive, corresponding to the five Carrington rotations presented in Fig. 1 from CR2064 (starting on 01.12.2007) to CR2068 (ending on 16.04.2008). One can clearly observe, in addition to the polar coronal holes, two low-latitude coronal holes throughout the whole study interval. These low-latitude CHs will be referred to as CH1 and CH2, and each (re)appearance is denoted in Fig. 2 as CH1-1, ..., CH1-5, and CH2-1, ..., CH2-5, respectively. The maps demonstrate that the location, polarity and overall size and shape of the two CHs remain rather invariant during this period. CH2 is considerably wider in longitude than CH1 and is located at low southern latitudes, while CH1 straddles around the equator. The locations, polarities and shapes of these two low-latitude CHs correspond to the properties of the two HSS/CIR sequences observed at 1 AU.

Assuming that the observed HSS solar wind speed of about 600-700 km/s (see Fig. 1a) remains roughly constant for most of the 1 AU distance, the average time delay of an HSS/CIR event is about 2-3 days. Using this time delay, the similar polarities and solar wind profiles at 1AU, and the size, shape and location of the observed CHs, we conclude that the HSS/CIR events of sequence 1 (2) originate from CH1 (CH2, respectively).

Figure 3 shows a stack plot of equatorial slices (heliolatitudes of ± 40 deg) extracted from McIntosh coronal hole maps during CR2059 - CR2073. Figure 3 depicts the evolution of the equatorial CHs before, during and after the study period. Lower and upper horizontal lines indicate the starting and ending times of the study (CR2064-CR2069), respectively. One can see that CH1 and CH2 appeared even before and after the study period, but suffered considerable changes in time. There are also other coronal hole sequences outside the time interval of our study. For example, during the previous rota-

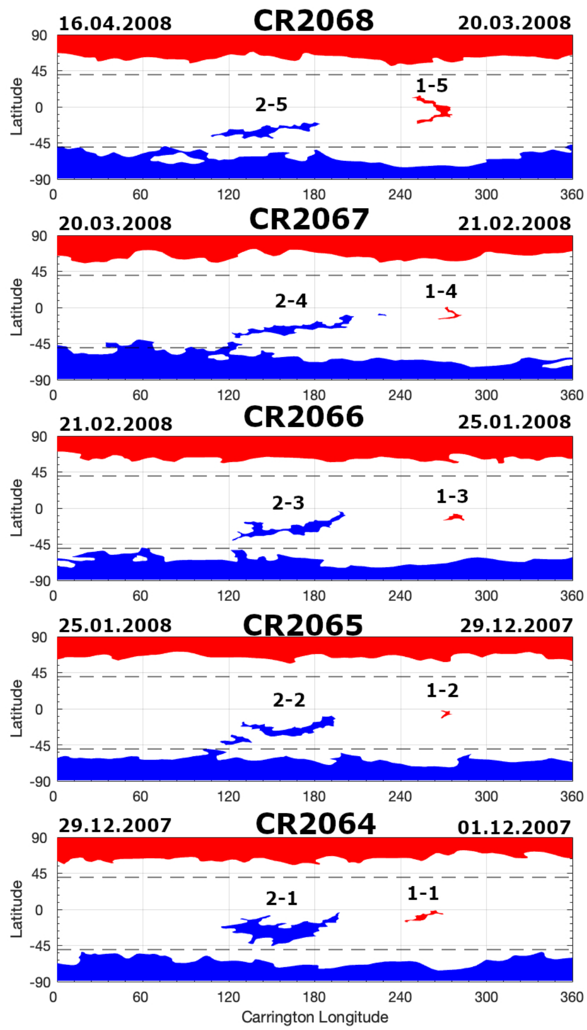

Figure 2. Carrington maps of the McIntosh Archive during December 2007 - April 2008. From top to bottom: CR2068, CR2067, CR2066, CR2065 and CR2064. Negative-polarity coronal holes are depicted in red, and the positive-polarity holes in blue. The x-axis shows the Carrington heliolongitude and the y-axis the heliolatitude.

tions, one observes the presence of an additional negative-polarity coronal hole at a longitude of about 0 degrees. This is the source of the weaker HSS sequence after sequence 2, even though the respective region is no longer identified as a coronal hole since CR2064.

5 Superposed epoch analysis

Here we compare the average properties of the two HSS/CIR sequences using the superposed epoch (SPE) method. We extract the measurements corresponding to each

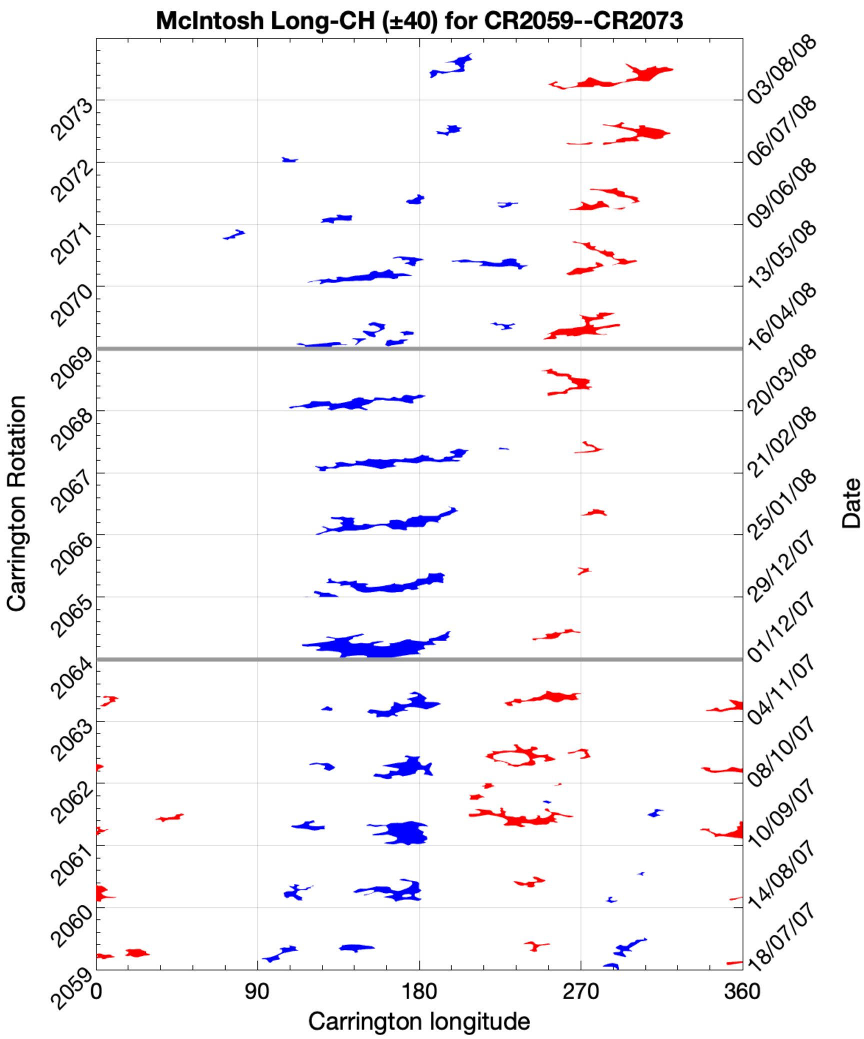

Figure 3. Stack plot of equatorial slices (±40 deg of heliolatitude) extracted from coronal hole maps of the McIntosh Archive during July 2007 - August 2008. Lower and upper solid horizontal lines indicate the starting and ending times of the study, respectively; weak horizontal lines separate the CRs. Five Carrington rotations were added before and after the study interval.

HSS/CIR event, superpose the time segments onto each other around the zero epoch day defined by the arrival of the leading edge of each event, and compute average time profiles. Figure 4 presents the results for the solar wind speed and density, the magnitude and the x, y and z components of the IMF (in GSE system). The superposed solar wind speed profiles (Fig. 4, panels a1 and a2) are fundamentally different for the two sequences. The HSS/CIR events of sequence 1 are overall much shorter than those of sequence 2, with an average duration of 5.86 days, as compared to the average 8.66-day duration of the sequence 2 events. Note that colour in Fig. 4 indicates the duration of the shortest HSS/CIR event in each sequence (5.42 days for sequence 1, and 7.29 days for sequence 2). The maximum SPE speed of sequence 1 appears to be slightly lower than for sequence 2. However, there is more scatter in the profile and maximum speed among the events of sequence 1 than sequence 2.

The superposed solar wind density profiles for the two sequences (Fig. 4, panels b1 and b2) are also somewhat different. The SPE peak density is slightly higher for sequence 1 than sequence 2. This is most likely related to the slightly faster rise of the mean solar wind speed profile, which better synchronises the density peaks for sequence 1 in the SPE process. There is also more variability between the density peaks of sequence 2 events, where two peaks remain below 20 cm^{-3} while they also include the highest peak (HSS/CIR2-1) of all ten events (see Fig. 1b).

The superposed IMF magnitude (Fig. 4, panels c1 and c2) follows quite closely the profile of the density in each sequence. The SPE mean IMF magnitude rises to a maximum of about 10 nT at the start of each sequence, but the rise is slightly faster in sequence 1. After day 2, the average B of sequence 2 remains at a closely constant value of about 5 nT up to the end of the interval. On the other hand, the average B of sequence 1 continues to decrease even after day 2, reaching a minimum value of about 2.5 nT on day 5.

The IMF polarity can be determined from the Bx or By component of the IMF, with positive polarity (away sector) defined by $Bx < 0$ or $By > 0$, and negative polarity (toward sector) by $Bx > 0$ or $By < 0$. For sequence 1, both Bx and By (Fig. 4, panels d1 and e1) depict the same change of IMF polarity from a (slightly favoured) away sector before the epoch zero time (start of sequence 1) to a well-defined toward sector. The opposite change is seen for sequence 2 (Fig. 4, panels d2 and e2), which has a dominant away sector polarity. Because of the great variability of the IMF Bz-component (see Fig. 1d), the superposed profiles (Fig. 4, panels f1 and f2) are rather random.

6 Geomagnetic activity

Figure 5 shows the geomagnetic AE and SYM-H indices during our study interval. Figure 5 highlights that each HSS/CIR event produces strong high-latitude activity (substorms) as depicted by the AE index and a minor storm, as shown by the SYM-

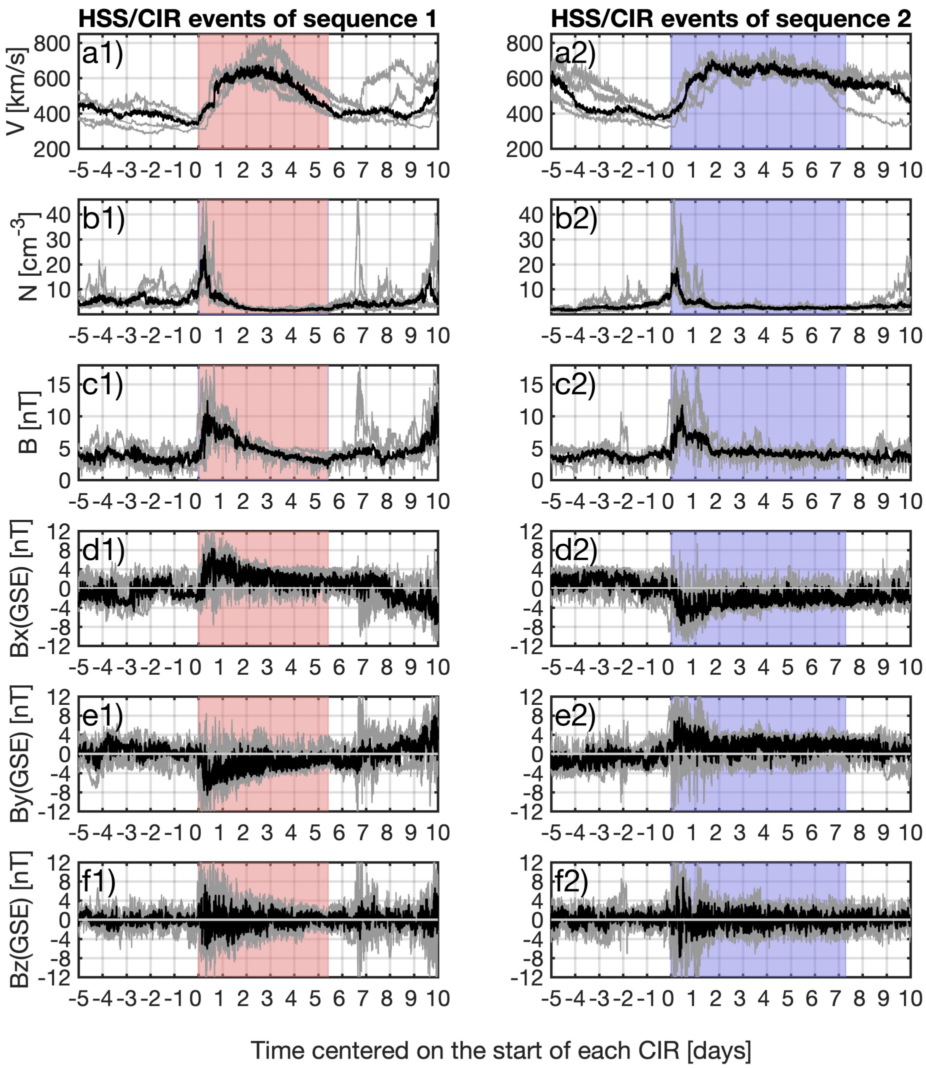

Figure 4. Left: Superposed epoch analysis of the 5 HSS/CIR events of sequence 1. Right: The same for sequence 2. From top to bottom: solar wind speed, solar wind density, IMF magnitude, and the IMF Bx(GSE), By(GSE) and Bz(GSE) components. Individual HSS/CIR events are depicted in grey and the black line gives the superposed average. x-axis gives the day number around the zero epoch day, from day -5 to day 10.

H index. The AE index (Fig. 5a) shows large values at the beginning of each HSS/CIR event, i.e., at the main phase of the corresponding storm, with AE values decreasing during the storm recovery phase. Compared to SYM-H, the AE index shows much larger variability, with multiple intermittent spikes (characteristic for substorms) distributed

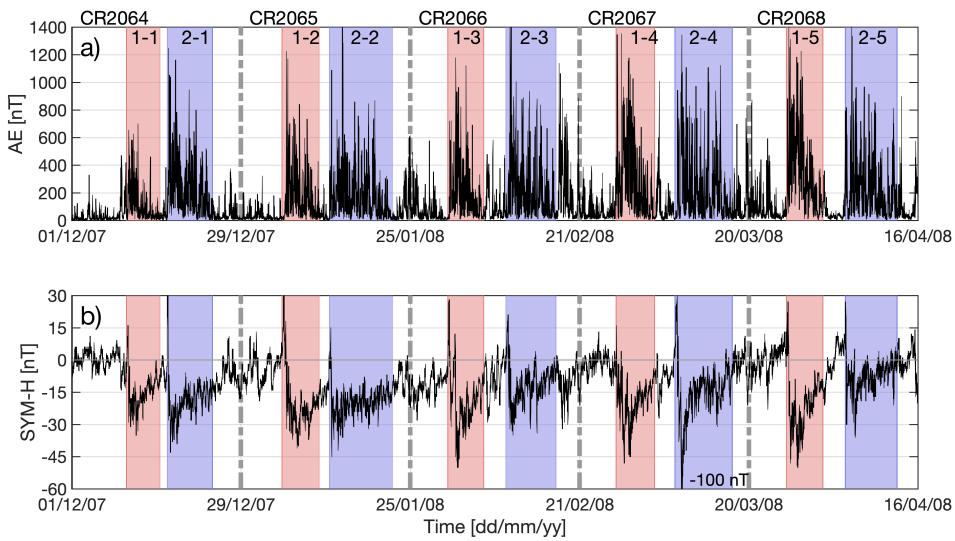

Figure 5. Geomagnetic activity indices during December 2007 - April 2008. Top: AE index; bottom: SYM-H index.

throughout the storm interval. The SYM-H index (Fig. 5b) shows the structure of a magnetic storm: the initial brief increase (compression), followed by a rapid decrease (main phase), and then a slow return to undisturbed values (recovery phase). In each event, the SYM-H index decreases below -30 nT but remains mostly above -50 nT, i.e. within the limit of a minor storm. Only HSS/CIR2-4 generates a moderate storm with minimum SYM-H index equal to -100 nT.

Figure 6 depicts the superposed epoch analysis of the two geomagnetic indices separately for the two sequences. The SPE time profiles of the AE index (Fig. 6, panels a1 and a2) show significant differences between the two sequences. The index shows a more systematic increase on days 0 and 1 for sequence 1, although the maxima on day 1 are roughly equally high for both sequences. Even more clearly, the mean AE index stays considerably higher after the maximum on days 1 and 2 for sequence 1. The mean level of days 0-2 is about 340 nT for sequence 1 and about 262 nT for sequence 2. The largest difference in the mean AE index between the two sequences is seen on day 2, where the mean values are around 400 nT for sequence 1 and around 200 nT for sequence 2.

The SPE time profiles of the SYM-H index (Fig. 6, panels b1 and b2) are also different for the two sequences. The start of the main phase (initial decline of SYM-H) is slightly more systematic and steep in sequence 1. Even more clearly, the period of low-

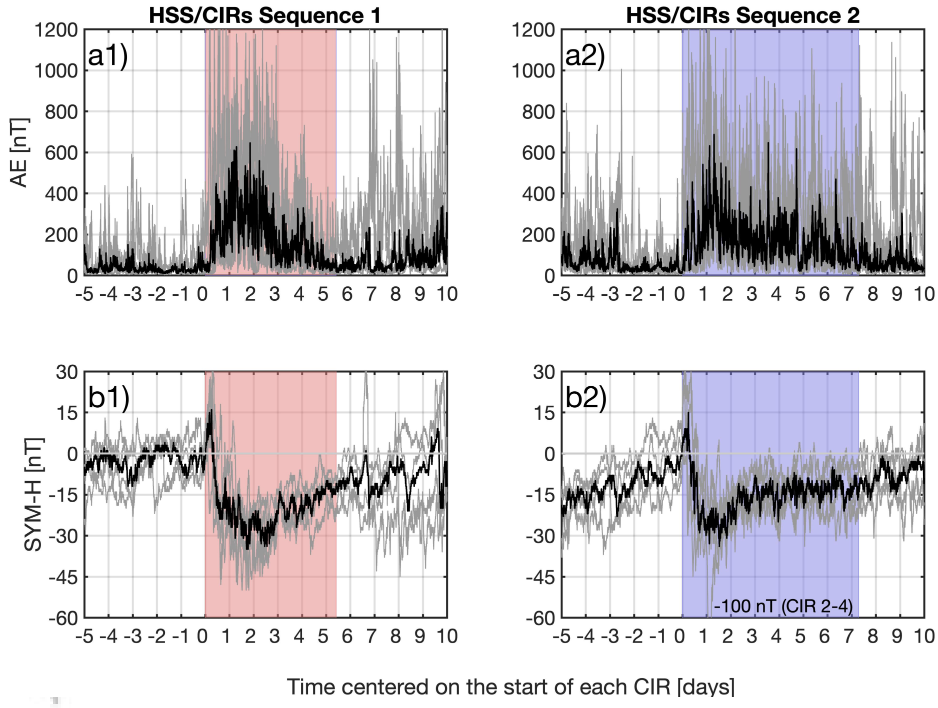

Figure 6. Superposed epoch analysis of geomagnetic disturbances triggered by the ten HSS/CIR events marked in Figs. 1 and 5. Top: AE index; bottom: SYM-H index.

est index values (the main phase of storm) lasts to day 2 for sequence 1, roughly one day longer than for sequence 2. These differences in SYM-H correspond very well to the simultaneous differences in the AE index between the two sequences. The storm recovery of sequence 2 starts in the middle of day 1 and reaches the level of -15 nT on day 2. The recovery phase of sequence 1 starts one day later and the -15 nT level is reached only on day 4.

7 Estimating the Russell-McPherron effect

When studying solar wind streams with opposite IMF polarities, the Russell-McPherron (R-M) effect is often invoked as one factor to explain the observed differences in the geo-effectiveness of the streams. In this section we will quantify the R-M effect, by showing not only that the effect is mainly responsible for those differences in the average geoactivity of the two HSS/CIR sequences shown in Fig. 6, but also that the effect, as expected, evolves in time, becoming stronger as we approach the spring of 2008. We also note that, in addition to the R-M mechanism, the other mechanism that contributes largely to the semiannual variation of geomagnetic activity is the equinoctial hypothesis (Lyatsky et al., 2001; Cliver et al., 2000). At equinox, when the nightside auroral zones of both hemispheres are in darkness, ionospheric conductivity is reduced. This reduces the currents required to complete the solar wind-magnetosphere-ionosphere coupling, but the corresponding electric fields are enhanced, which increases the activity level (Lyatsky et al., 2001). Moving now from (northern) winter solstice to spring equinox, the reducing solar illumination in the summer (southern) hemisphere enhances the global night-side sensitivity to solar wind driving. However, this change affects the HSS/CIR events of opposite polarities equally, thus leaving the R-M effect as the dominant mechanism of causing differences between the two, roughly simultaneous HSS/CIR events of each rotation.

The direction of the IMF is often specified using two complementary coordinate systems: 1) the geocentric solar ecliptic (GSE), where the x-axis points from the center of the Earth towards the Sun, the z-axis is positive in the direction of the normal to the ecliptic plane, and the y-axis completes the right-handed system; and 2) the geocentric solar magnetospheric (GSM), where the x-axis is the same as in GSE, the z-axis is in the direction of the projection of the dipole axis onto the GSE y-z plane, and the y-axis completes the right-handed system. Note that the only difference between the GSE and GSM frames consists in a rotation about the x-axis, with the angle of rotation referred to in the following as θ.

It can be shown that the IMF Bz(GSM) component is connected to By(GSE) and Bz(GSE) components by (e.g. Kivelson & Russell, 1995; Lockwood et al., 2016):

$$Bz(GSM) = sin(\theta) \times By(GSE) + cos(\theta) \times Bz(GSE) \tag{1}$$

The angle of rotation, θ, between the GSE and GSM coordinate systems, has both an annual ($\pm 23.5°$) and a diurnal ($\pm 11°$) variation, and is defined as positive in the clockwise direction when the Earth is viewed from the Sun. Each year in spring, θ varies between $+23.5° + 11° = 34.5°$ at 22 UT and $+23.5° - 11° = 12.5°$ at 10 UT. Thus, $sin(\theta)$ is always positive in spring and, according to Eq. 1, assuming that Bz(GSE) ≈ 0, a negative (duskward) By(GSE) gives rise to a negative Bz(GSM). Similarly, a positive (dawnward) By(GSE) gives rise to a positive Bz(GSM) in spring. Conversely, in fall, θ varies between $-23.5° + 11° = -12.5°$ at 22 UT and $-23.5° - 11° = -34.5°$ at 10 UT, thus $sin(\theta)$ is always negative in fall. Then, according to Eq. 1, a negative By(GSE) gives rise to a positive Bz(GSM) and a positive By(GSE) gives rise to a negative Bz(GSM). Around solstices, when the Earth's rotational axis points away or toward the Sun, θ varies between $-11°$ to $+11°$ (θ vanishes at 4 and 16 UT), thus, By(GSE) has little effect on Bz(GSM).

In this study, the R-M effect is expected to be quite minor at the start of the study interval, close to the winter solstice of 2007, and is expected to increase towards the end of the interval close to the spring equinox of 2008. Since the R-M effect is polarity-dependent, the negative-polarity sequence 1 events are expected to become increasingly geoeffective towards the end of our study interval. As shown in Eq. 1, the Bz(GSM) component also depends on Bz(GSE), which, for this study, can be considered to be due to random fluctuation. Therefore, in order to remove the influence of such random fluctuations, we use the difference Bd = Bz(GSM) - Bz(GSE).

Figure 7 depicts the temporal evolution of the R-M effect as revealed by Bd. One can clearly see the turning on of the R-M effect in both sequences as we advance in time towards the spring. Figure 7 shows how the mean value of Bd during sequence 1 decreases from roughly zero (or slightly positive) during CR2064 (December 2007), to increasingly negative values during CR2067 (February 2008) and CR2068 (March 2008). This demonstrates the increasing effect of the R-M mechanism in the IMF toward sector as we move from winter solstice to the spring equinox. Moreover, there is an opposite effect on sequence 2: the mean value of Bd increases from roughly zero (or slightly negative) during CR2064 to increasingly positive values during CR2067 and CR2068.

In Fig. 8 we plot the probability density functions (PDFs) of the values of Bz(GSM), Bd, AE and SYM-H during each HSS/CIR event. (To obtain the PDF, a given set of values is first partitioned into a uniform set of bins covering the full range of values. The PDF is then obtained by dividing the number of values inside each bin by the total number of values and by the width of the bin.) In order to avoid the excessive variability of values during the compression phase (the actual CIR), we included the values of the four variables only during days 1-3 within the PDFs of Fig. 8. This 3-day interval corresponds to the end of the main phase and the recovery phase of the related storms (see Fig. 6). Note also that the sector structure, as determined by the Bx(GSE) and By(GSE) components (see Fig. 4) is most clearly ordered during these 3 days, thus maximising the R-M effect.

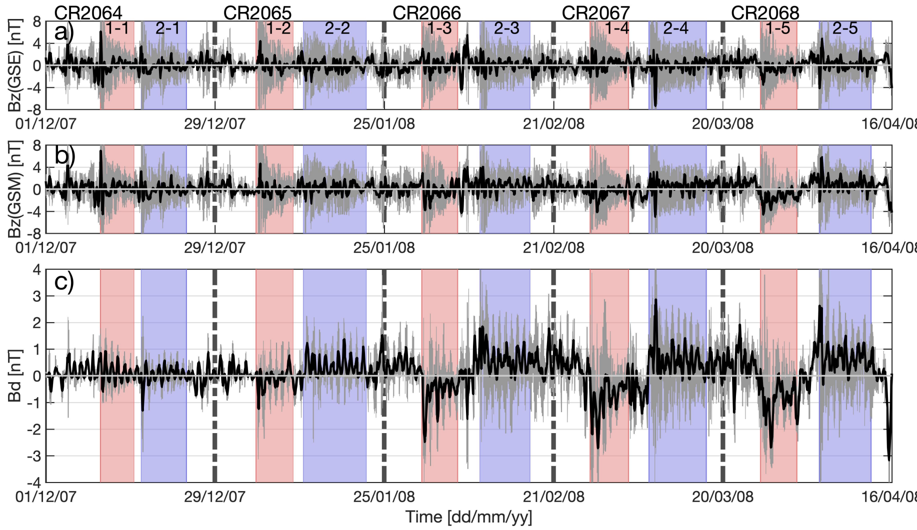

Figure 7. Temporal evolution of the IMF Bz component. From top to bottom: Bz(GSE) component, Bz(GSM) component and their difference Bd = Bz(GSM) - Bz(GSE). The 1-min resolution data is depicted in grey and the black line is its 6-hour running mean curve.

Figure 8 (panels a1-e1) shows a systematic decrease (increase) of the median values of the IMF Bz(GSM) component during the HSS/CIR events of sequence 1 (sequence 2, respectively) from +0.45 nT (-0.53 nT) for HSS/CIR1-1 (HSS/CIR2-1) to -1.74 nT (+0.92 nT) for HSS/CIR1-5 (HSS/CIR2-5). These changes are in a good agreement with the corresponding changes in the Bd difference (Fig. 8, panels a2-e2) and the turning on of the R-M effect. However, in addition to the R-M effect, the Bz(GSM) values (and related geoefficiency) include the effect of random fluctuations. Note first that the median value of Bz(GSM) during HSS/CIR1-1 is positive but negative during HSS/CIR2-1 (Fig 8, panel a1), and the difference in Bz(GSM) between these two streams is larger than predicted by the R-M effect (small values of Bd in Fig. 8, panel a2). Accordingly, the large difference in Bz(GSM) between HSS/CIR1-1 and HSS/CIR2-1, and the related differences in geomagnetic effects (see Fig. 5), are due to other processes, most likely the random fluctuations during the compression phase.

Note also the strong negative Bz(GSE) component at the start of the HSS/CIR2-4 event (see Fig. 7a), which is responsible for the largest geomagnetic storm in our study interval (minimum SYM-H of -100 nT). In this case, even though the R-M mechanism acts to raise the Bz(GSM) component (see Fig. 7b) to be less negative (less geoeffective),

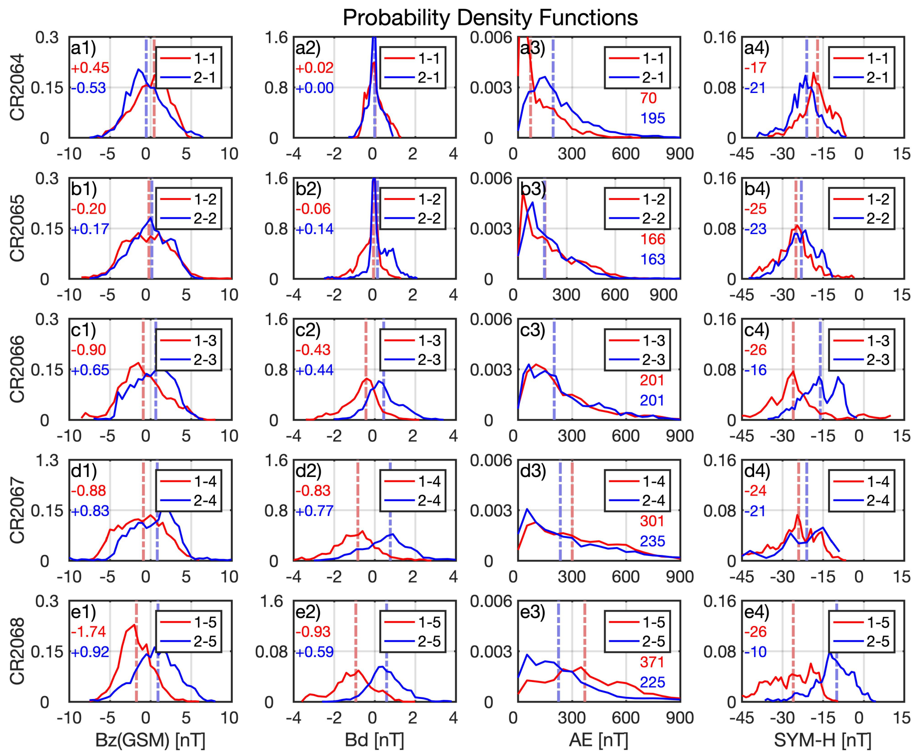

Figure 8. Temporal evolution of the R-M effect using probability density functions. Columns from left to right: IMF Bz(GSM) component, Bd, AE index and SYM-H index. Rows from top to bottom: CR2064, CR2065, CR2066, CR2067, CR2068. Colours have the same meaning as in previous figures: red (blue) for sequence 1 (sequence 2). Each panel depicts the PDFs for the two HSS/CIR events within the same Carrington rotation. Coloured numbers give their median values, also depicted as vertical lines.

the large negative Bz(GSE) still dominates the Bz(GSM) and the geomagnetic effect of this HSS/CIR event. Accordingly, the HSS/CIR2-4 event, which has a R-M non-geoeffective polarity, is in fact more geoeffective that the HSS/CIR1-4 event, which is R-M geoeffective. This shows that the R-M effect is, despite its systematic nature, often rather small against other forms of variability that affect the difference between individual events. This is also the reason why evidence for the R-M effect has, until the current study, largely remained to be based on statistical studies of different geomagnetic activity variables.

Figure 8 (panels a3-e3) show a systematic increase of the median value of the AE index for sequence 1, but not for sequence 2. This is in line with the R-M effect, which predicts an increase of geomagnetic activity for negative-polarity solar wind streams as we approach the March equinox. The median value of AE for sequence 1 increases from 70 nT during CR2064 to 371 nT during CR2068. On the other hand, the median values of AE for sequence 2 are rather constant, around 200 nT for all events. Note that the high-latitude geomagnetic activity associated with the HSS/CIR1-1 event is much weaker than that associated with HSS/CIR2-1, supporting the above discussed difference in the corresponding Bz(GSM) values. Note also that, even though the HSS/CIR2-4 event generated the strongest storm during this period, the median AE index of HSS/CIR2-4 is 235 nT, weaker than the median AE index of HSS/CIR1-4 (301 nT). This is due to the short duration of the strong Bz(GSM) interval of HSS/CIR2-4 (see Fig. 7), which creates a deep but short storm main phase (see Fig. 5).

Figure 8 (panels a4-e4) show that, starting from CR2065, the median values of SYM-H for the sequence 1 events are slightly more negative than those of sequence 2. During CR2064, the opposite relation is valid, and the HSS/CIR2-1 event leads to a stronger storm than HSS/CIR1-1 (see Fig. 5). This is due to its more negative Bz(GSM) component, as discussed above. Figure 8 (panel d4) shows that, even though the main phase of the geomagnetic storm associated with HSS/CIR2-4 was the strongest in our dataset, the median value of the SYM-H index of HSS/CIR1-4 (-24 nT) was slightly below that of HSS/CIR2-4 (-21 nT).

8 Summary and Conclusions

We have studied here the high-speed streams and the associated corotating interaction regions that were observed at 1 AU in December 2007 - April 2008 (CR2064 to CR2068). We identified two HSS/CIR sequences during this period, with the related HSS/CIR events repeating almost unchanged during the five solar rotations. We showed that these two sequences had oppositely oriented IMF polarities, and that they were generated by two persistent low-latitude coronal holes with corresponding polarities. The time delays between successive events, the similar solar wind profiles and polarities at 1AU, and also the overall size, shape and location of the observed CHs, were used in the identification of the corresponding CH sources. We showed that the location, polarity and overall size and shape of the two CHs, remain rather invariant during the study period. Although the two CHs were observed even before and after the study period, they suffered considerable changes during the previous and subsequent rotations, thus limiting the stable time interval to the five solar rotations included in our study. The sequence of negative-polarity HSS/CIR events was denoted by sequence 1, and the sequence of positive-polarity HSS/CIR events, by sequence 2, respectively.

We used the superposed epoch analysis to study the average properties of the solar wind and IMF during the events of these two sequences separately. We showed that the superposed solar wind speed profiles were fundamentally different for the two sequences in the following way: the events of sequence 1 were clearly shorter than those of sequence 2, with an average duration of 5.86 days compared to the average 8.66-day duration of the events of sequence 2. The superposed solar wind density and IMF magnitude profiles were found to be more similar for the two sequences than the speed profiles. The superposed profiles of the IMF Bx and By components verified the clear toward (away) sector polarity of sequence 1 (sequence 2). There was also evidence for a change in sector structure, with opposite polarity dominating a couple of days before the superposed epoch zero time. This pattern was more systematic in sequence 2.

Superposed epoch analysis was also used to study the average effects to high-latitude geomagnetic activity and to geomagnetic storms. We showed that the SPE time profiles for both AE and SYM-H indices were quite different for the two sequences. The mean AE level of SPE days 0-2 was about 340 nT for sequence 1 and about 262 nT for sequence 2. The largest difference in the mean AE index was seen on SPE day 2, where the mean values were around 400 nT for sequence 1 and around 200 nT for sequence 2. The period of lowest SPE values for the SYM-H index, i.e. the storm main phase, lasted up to the SPE day 2 for sequence 1, roughly one day longer than for sequence 2. The storm recovery of sequence 2 started in the middle of SPE day 1 and reached the level of -15 nT on SPE day 2. The recovery phase of sequence 1 started one SPE day later and the -15 nT level was reached only on day 4.

We followed the temporal evolution of the IMF Bz(GSE) and Bz(GSM) components from the first to the last HSS/CIR event within the two sequences separately. We found a systematic decrease of the Bz(GSM)-Bz(GSE) difference in sequence 1 and a systematic increase of this difference in sequence 2, when moving from the first rotation (CR2064) around the winter solstice of 2007 until the rotation CR2068 around the spring equinox 2008. These changes offer the first detailed, quantitative monitoring of the onset (turning on) of the effect of the Russell-McPherron mechanism from its minimum around the (winter) solstice to its maximum soon after the (spring) equinox (Russell & McPherron, 1973).

We made a detailed analysis of the probability distributions of the values of the Bz(GSM)-Bz(GSE) difference and the AE and SYM-H indices for each rotation separately and studied their change from the first to the last rotation in order to accurately quantify the R-M effect to geomagnetic activity and storminess. Geomagnetic activity of sequence 1 was shown to systematically increase relative to sequence 2 as a consequence of the turning on of the R-M effect. In particular, the median value of the AE index of sequence 1 increased systematically from 70 nT during CR2064 to 371 nT during CR2068, while the AE index of sequence 2 showed no systematic trend. The median value of the SYM-H index of sequence 1 during the first rotation was higher (less geoeffective) than for sequence 2 but, in the later rotations, the SYM-H index of sequence 1 became clearly more negative (more geoeffective) than for sequence 2. These changes are in a good agreement with the R-M effect, which predicts an increase (decrease) of geomagnetic activity for negative (positive) polarity solar wind streams as we approach the spring equinox.

Concluding, the two long-lived, low-latitude coronal holes observed during 2007-2008 generated the two high-speed stream sequences observed at 1 AU that were responsible for the recurrent geomagnetic activity examined in this study. (Note that our study also includes the one-month interval of the international WHI study). We presented the first detailed analysis of the systematic evolution ("turning on") of the R-M mechanism with opposite effects to the two HSS/CIR sequences of opposite polarity. The detailed monitoring of the R-M effect was made possible by the extremely stable (quiet) solar conditions, reducing the level of random changes in solar wind/IMF parameters and allowing the HSS/CIR events in both sequences to repeat almost unchanged. These conditions were optimal, probably even unique so far, for such a repeated experiment in the natural laboratory of the solar-terrestrial environment. The geomagnetic effects of the two HSS/CIR sequences were only moderate, with medium-size high-latitude disturbances and, mostly, minor storms, roughly of the same maximum strength for both sequences. However, the R-M mechanism systematically affected the IMF Bz(GSM) component of the two HSS/CIR sequences, increasing (decreasing) the geoeffectiveness of the negative (positive) polarity HSS/CIR streams. The R-M effect did not greatly modify the maximum intensity of the storm caused by the R-M geoeffective stream, but rather prolonged its main phase by delaying the start of the recovery phase up to day 3 after the start of the storm.

We note that, while there are hundreds of papers discussing the R-M mechanism statistically, and some papers even discussing the R-M mechanism in individual events, there is no previous study to show the systematic, opposite development of the IMF Bz-component in two HSS streams of opposite polarity and the related oppositely developing changes in geomagnetic activity. In this paper, by following the repetition of two HSSs during five successive rotations, we are able to follow the onset ("turning on") of the R-M effect in the two streams with opposite polarities and with opposite changes in the Bz-components. In this way we can demonstrate that the observed, systematically different changes in geomagnetic activity are indeed due to the oppositely changing Bz-components of the two streams, and not due to the other geoeffective factors in solar wind. The repetition of the two HSSs almost unchanged during five solar rotations is probably unique in space history (at least in space literature) and is due to the fact that solar activity was very quiet at this time, only some months before the exceptionally low and long sunspot minimum.

Acknowledgments

We acknowledge the financial support by the Academy of Finland to the ReSoLVE Centre of Excellence (project 307411), and by the Romanian Ministry of National Education (VESS project, number 18PCCDI/2018). The Carrington maps were downloaded from the McIntosh Archive (Patrick S. McIntosh, NOAA Space Environment Laboratory (1964). Synoptic Maps Composites Observed from McIntosh. NOAA National Centers for Environmental Information. doi:10.7289/V5765CCQ [January 2019]). Solar wind parameters and geomagnetic indices were downloaded from: https://omniweb.gsfc.nasa.gov.

References

Abramenko, V., Yurchyshyn, V., Linker, J., Mikic, Z., Luhmann, J., & Lee, C. O. (2010). Low-latitude coronal holes at the minimum of the 23rd solar cycle. *The Astrophysical Journal*, *712*, 813-818. doi: 10.1088/0004-637X/712/2/813

Alves, M. V., Echer, E., & Gonzalez, W. D. (2006). Geoeffectiveness of corotating interaction regions as measured by Dst index. *J. Geophys Res.*, *111*, A07S05.

doi: 10.1029/2005JA011379

Bartels, J. (1932). Terrestrial magnetic activity and its relation to solar phenomena. *Terr. Magn. Atmos. Electr.*, *37*(1), 1-52.

Bohlin, J. D. (1977). Extreme-ultraviolet observations of coronal holes. I. Locations, size and evolution of coronal holes, June 1973-January 1974. *Sol. Phys.*, *51*, 377-398. doi: 10.1007/BF00216373

Boller, B. R., & Stolov, H. L. (1970). Kelvin-Helmholtz instability and the semiannual variation of geomagnetic activity. *J. Geophys. Res.*, *75*, 6073-6084. doi: 10.1029/JA075i031p06073

Cliver, E. W., Kamide, Y., & Ling, A. G. (2000). Mountains versus valleys: Semiannual variation of geomagnetic activity. *J. Geophys. Res.*, *105*(A2), 2413-2424. doi: 10.1029/1999JA900439

Cortie, A. L. (1912). Sun-spots and Terrestrial Magnetic Phenomena, 1898-1911: the Cause of the Annual Variation in Magnetic Disturbances. *Mon. Not. R. Astron. Soc.*, *73*, 52-60. doi: doi.org/10.1093/mnras/73.1.52

Crooker, N. U. (2000). Solar and heliospheric geoeffective disturbances. *Journal of Atmospheric and Solar-Terrestrial Physics*, *62*, 1071-1085. doi: 10.1016/S1364-6826(00)00098-5

Crooker, N. U., & Cliver, E. W. (1994). Postmodern view of m-regions. *Journal of Geophysical Research*, *99*. doi: 10.1029/94JA02093

Davis, T. N., & Sugiura, M. (1966). Auroral electrojet activity index AE and its universal time variations. *Journal of Geophysical Research*, *71*(3), 785-801. doi: 10.1029/JZ071i003p00785

de Toma, G. (2011). Evolution of coronal holes and implications for high-speed solar wind during the minimum between cycles 23 and 24. *Solar Phys.*, *274*, 195-217. doi: 10.1007/s11207-010-9677-2

Dungey, J. W. (1961). Interplanetary magnetic field and the auroral zones. *Physical Review Letters*, *6*(2), 47-48. doi: 10.1103/PhysRevLett.6.47

Echer, E., Tsurutani, B. T., Gonzalez, W. D., & Kozyra, J. U. (2011). High Speed Stream Properties and Related Geomagnetic Activity During the Whole Heliosphere Interval (WHI): 20 March to 16 April 2008. *Sol. Phys.*, *274*(1-2), 303-320. doi: 0.1007/s11207-011-9739-0

Gibson, S. E., de Toma, G., Emery, B., Riley, P., Zhao, L., Elsworth, Y., … Webb,

D. (2011). The Whole Heliosphere Interval in the context of a long and structured solar minimum - An overview from Sun to Earth. *Solar Phys.*, *274*, 5-27. doi: 10.1007/s11207-011-9921-4

Gibson, S. E., Kozyra, J. U., de Toma, G., Emery, B. A., Onsager, T., & Thompson, B. J. (2009). If the Sun is so quiet, why is the Earth ringing? A comparison of two solar minimum intervals. *J. Geophys. Res.*, *114*, A09105. doi: 10.1029/2009JA014342

Gosling, J. T., & Pizzo, V. J. (1999). Formation and evolution of corotating interaction regions and their three dimensional structure. In A. Balogh, J. T. Gosling, J. R. Jokipii, R. Kallenbach, & H. Kunow (Eds.), *Corotating Interaction Regions.* Space Sciences Series of ISSI, vol 7., Springer, Dordrecht. doi: 10.1007/978-94-017-1179-1_3

Hajra, R., Echer, E., Tsurutani, B. T., & Gonzalez, W. D. (2013). Solar cycle dependence of High-Intensity Long-Duration Continuous AE Activity (HILDCAA) events, relativistic electron predictors? *J. Geophys. Res.*, *118*, 5626-5638. doi: 10.1002/jgra.50530

Holappa, L., Mursula, K., & Asikainen, T. (2014). A new method to estimate annual solar wind parameters and contributions of different solar wind structures to geomagnetic activity. *J. Geophys. Res. Space Physics*, *119*, 9407-9418. doi: 10.1002/2014JA020599

Iyemori, T., Takeda, M., Nose, M., Odagi, Y., & Toh, H. (2010). Mid-latitude Geomagnetic Indices ASY and SYM for 2009 (Provisional). *Internal Report of Data Analysis Center for Geomagnetism and Space Magnetism, Kyoto University, Japan.* Retrieved from {http://wdc.kugi.kyoto-u.ac.jp/aeasy/asy.pdf}

Kilpua, E. K. J., Balogh, A., von Steiger, R., & Liu, Y. D. (2017). Geoeffective properties of solar transients and stream interaction regions. *Space Sci. Rev.*, *212*, 1271-1314. doi: 10.1007/s11214-017-0411-3

Kivelson, M. G., & Russell, C. T. (1995). *Introduction to Space Physics.* Cambridge University Press, ISBN: 9780521457149.

Lei, J., Thayer, J. P., Wang, W., & McPherron, R. L. (2011). Impact of CIR storms on thermosphere density variability during the solar minimum of 2008. *Solar Phys.*, *274*, 427-437. doi: 10.1007/s11207-010-9563-y

Lockwood, M., Owens, M. J., Barnard, L. A., Bentley, S., Scott, C. J., & Watt, C. E. (2016). On the origins and timescales of geoeffective IMF. *Space Weather*, *14*, 406-432. doi: 10.1002/2016SW001375

Lyatsky, W., Newell, P. T., & Hamza, A. (2001). Solar Illumination as Cause of the Equinoctial Preference for Geomagnetic Activity. *Geophys. Res. Lett.*, *28*(12), 2353-2356. doi: 10.1029/2000GL012803

Maris, G., & Maris, O. (2009). WHI high-speed streams at geospace. *Proceedings of the International Astronomical Union*, *5*(H15), 494-497. doi: 10.1017/S1743921310010379

Mason, G. M., Desai, M. I., Mall, U., Korth, A., Bucik, R., von Rosenvinge, T. T., & Simunac, K. D. (2009). In situ observations of CIRs on STEREO, Wind, and ACE during 2007-2008. *Solar Phys.*, *256*, 393-408. doi: 10.1007/s11207-009-9367-0

McGranaghan, R., Knipp, D. J., McPherron, R. L., & Hunt, L. A. (2014). Impact of equinoctial high-speed stream structures on thermospheric responses. *Space Weather*, *12*, 277-297. doi: 10.1002/2014SW001045

McIntosh, D. H. (1959). On the Annual Variation of Magnetic Disturbance. *R. Soc. London Philos. Trans., Ser. A*, *251*, 525-552. doi: 10.1098/rsta.1959.0010

McPherron, R. L., Baker, D. N., & Crooker, N. U. (2009). Role of the Russell-McPherron effect in the acceleration of relativistic electrons. *Journal of Atmospheric and Solar-Terrestrial Physics*, *71*(10), 1032-1044. doi: https://doi.org/10.1016/j.jastp.2008.11.002

Miyoshi, Y., Kataoka, R., Kasahara, Y., Kumamoto, A., Nagai, T., & Thomsen, M. F. (2013). High-speed solar wind with southward interplanetary magnetic field causes relativistic electron flux enhancement of the outer radiation belt via enhanced condition of whistler waves. *Geophys. Res. Lett.*, *40*, 4520-4525. doi: 10.1002/grl.50916

Mursula, K., Tanskanen, E., & Love, J. J. (2011). Spring-fall asymmetry of substorm strength, geomagnetic activity and solar wind - Implications for semiannual variation and solar hemispheric asymmetry. *Geophys. Res. Lett.*, *38*(L06104). doi: 10.1029/2011GL046751

Newell, P. T., Sotirelis, T., Skura, J. P., Meng, C. I., & Lyatsky, W. (2002). Ultraviolet insolation drives seasonal and diurnal space weather variations. *J. Geo-*